

## Intermodel Diversity of Simulated Long-term Changes in the Austral Winter Southern Annular Mode: Role of the Southern Ocean Dipole

Fei ZHENG<sup>1</sup>, Jianping LI<sup>2,3</sup>, and Shuailei YAO<sup>1</sup>

<sup>1</sup>*State Key Laboratory of Numerical Modeling for Atmospheric Sciences and Geophysical Fluid Dynamics, Institute of Atmospheric Physics, Chinese Academy of Sciences, Beijing 10029, China*

<sup>2</sup>*Frontiers Science Center for Deep Ocean Multispheres and Earth System (FDOMES)/Key Laboratory of Physical Oceanography/Institute for Advanced Ocean Studies, Ocean University of China, Qingdao 266100, China*

<sup>3</sup>*Laboratory for Ocean Dynamics and Climate, Pilot Qingdao National Laboratory for Marine Science and Technology (QNLM), Qingdao 266100, China*

(Received 21 July 2020; revised 8 October 2020; accepted 20 October 2020)

### ABSTRACT

The Southern Annular Mode (SAM) plays an important role in regulating Southern Hemisphere extratropical circulation. State-of-the-art models exhibit intermodel spread in simulating long-term changes in the SAM. Results from Atmospheric Model Intercomparison Project (AMIP) experiments from 28 models archived in CMIP5 show that the intermodel spread in the linear trend in the austral winter (June–July–August) SAM is significant, with an intermodel standard deviation of  $0.28 (10 \text{ yr})^{-1}$ , larger than the multimodel ensemble mean of  $0.18 (10 \text{ yr})^{-1}$ . This study explores potential factors underlying the model difference from the aspect of extratropical sea surface temperature (SST). Extratropical SST anomalies related to the SAM exhibit a dipole-like structure between middle and high latitudes, referred to as the Southern Ocean Dipole (SOD). The role of SOD-like SST anomalies in influencing the SAM is found in the AMIP simulations. Model performance in simulating the SAM trend is linked with model skill in reflecting the SOD–SAM relationship. Models with stronger linkage between the SOD and the SAM tend to simulate a stronger SAM trend. The explained variance is about 40% in the AMIP runs. These results suggest improved simulation of the SOD–SAM relationship may help reproduce long-term changes in the SAM.

**Key words:** Southern Annular Mode, Southern Ocean Dipole, intermodel spread, air–sea interactions

**Citation:** Zheng, F., J. P. Li, and S. L. Yao, 2021: Intermodel diversity of simulated long-term changes in the austral winter Southern Annular Mode: Role of the Southern Ocean Dipole. *Adv. Atmos. Sci.*, **38**(3), 375–386, <https://doi.org/10.1007/s00376-020-0241-1>.

### Article Highlights:

- Intermodel spread in long-term changes in the austral winter SAM are significant.
- Extratropical SST anomalies related to the SAM exhibit a dipole-like structure, referred to as the SOD (Southern Ocean Dipole).
- Models with stronger linkage between the SOD and the SAM tend to simulate a stronger SAM trend, and vice versa.

## 1. Introduction

The dominant mode of atmospheric circulation in the Southern Hemisphere extratropics is the Southern Annular Mode (SAM), which manifests itself as a meridional oscillation in sea level pressure (SLP) between the middle and high latitudes, accompanied by a north–south fluctuation of the eddy-driven westerly jet (Gong and Wang, 1999; Kid-

son and Watterson, 1999; Thompson and Wallace, 2000; Li and Wang, 2003). During a positive (negative) phase of the SAM, the polar vortex tends to be stronger (weaker) and the westerly jet usually shifts toward the Antarctic (tropics). The SAM is an atmospheric intrinsic mode, and the underlying dynamics involves eddy–zonal mean flow interaction (Hartmann and Lo, 1998; Lorenz and Hartmann, 2001; Zhang et al., 2012).

The austral summer (December–January–February, DJF) SAM exhibits a significant positive linear trend during the past half century, which is mainly attributed to Antarctic stratospheric ozone depletion (e.g., Thompson et al.,

\* Corresponding author: Fei ZHENG  
Email: zhengfei08@mail.iap.ac.cn

2011). In contrast, the austral winter (June–July–August, JJA) SAM experienced weaker long-term changes. Models archived in phase 5 of the Coupled Model Intercomparison Project (CMIP5) show noticeable intermodel spread in simulating the long-term changes in both the JJA and DJF SAM (e.g., Swart et al., 2015). The intermodel spread in the JJA SAM is comparable with that in DJF. The JJA SAM plays an important role in influencing Southern Hemisphere extratropical winter climate, including extratropical precipitation (Kidston et al., 2009; Lim et al., 2016), ocean surface waves (Marshall et al., 2018), New Zealand river flow (Li and McGregor, 2017), and Antarctic temperatures (Turner et al., 2005; Fogt et al., 2012). Investigating intermodel spread in simulating temporal variability in the JJA SAM ensures a promising simulation and projection of southern extratropical winter climate.

Studies related to the intermodel difference in the SAM trend involve the intermodel spread in the magnitude of the projected poleward shift of the Southern Hemisphere westerly jet, which has been demonstrated to be related to the simulation of the 20th century climatology (Kidston and Gerber, 2010). Models with the climatological jet position closer to the equator in the 20th century simulation tend to shift the jet further poleward under global warming. However, the variability in the position of the westerly jet, albeit related to, is not equal to the SAM variability (Swart et al., 2015). Examining factors responsible for the intermodel diversity in the SAM's long-term changes may provide information for improving simulation of the SAM.

Extratropical SST anomalies modulate the overlaying atmospheric baroclinicity (Lau and Nath, 1990; Kushnir et al., 2002), regulate the nonlinear eddy–zonal mean flow interaction (Li et al., 2006; Sen Gupta and England, 2007; Liu et al., 2015; Zheng et al., 2015), and thus influence the extratropical atmospheric circulation (Kang et al., 2008, 2009; Nakamura et al., 2008; Wu et al., 2009; Sampe et al., 2010; Wu and Zhang, 2011; Yang and Wang, 2011; Hu et al., 2016; Xiao et al., 2016). SST anomalies in the Southern Hemisphere middle and high latitudes tend to exhibit an out-of-phase relationship, which is referred to as the Southern Ocean Dipole (SOD) (Zheng et al., 2018). The positive phase of the SOD corresponds to warmer and cooler SST anomalies at around 40°S and 60°S, respectively, and vice versa. Evidence from atmospheric general circulation model (AGCM) simulations shows that the SOD is positively correlated with the SAM during austral winter, suggesting a potential influence of the SOD on the SAM. However, models differ in describing the response of the SAM to the SOD (Zheng et al., 2018). Whether the intermodel uncertainty in depicting the response of the SAM to the SOD contributes to the intermodel difference in the simulated linear trend in the SAM is explored in this study.

The paper is structured as follows: Section 2 introduces the data and methods. The intermodel diversity in the simulated linear trend in the JJA SAM is shown in section 3. Section 4 explores the role of the SOD in the intermodel

diversity. Discussion and conclusions are given in section 5.

## 2. Data and methods

### 2.1. Data

The configuration of AGCM runs provides a useful approach to evaluate responses of atmospheric circulation to SST anomalies. AMIP simulations from 28 AGCMs archived in CMIP5 are used in this study. The AMIP runs were constrained using historical SST, and external forcing such as carbon dioxide and ozone concentrations are as in the historical experiment (Taylor et al., 2012). The list of the 28 models is shown in Table 1, and each model is given a short name. Model outputs are interpolated to the same horizontal resolution ( $1.0^\circ \times 1.0^\circ$ ) before statistical analysis. The analysis period of the AMIP simulations covers 1979–2008, and the season of interest is austral winter (June–July–August, JJA).

To detect the spatial pattern of the observed SAM, atmospheric reanalysis data from ERA-Interim are employed. To explore the temporal variability of the observed SAM, the station-based index of the SAM proposed by Marshall (2003) is used, which is characterized by reliability in describing the temporal variability of the SAM, especially before the satellite era.

### 2.2. Statistical methods

Empirical orthogonal function (EOF) analysis is used in this study. The leading EOF pattern and principle component are referred to as EOF1 and PC1. The statistical significance for correlation/regression analysis is assessed by the two-tailed Student's *t*-test. Partial correlation is employed to estimate the linkage between two variables after linearly removing effects of the third variable. The intermodel standard deviation quantifies the intermodel spread.

According to the method proposed by Nan and Li (2003), the model-simulated SAM index (SAMI) is calculated as the difference in the normalized zonal-mean SLP between 40°S and 70°S. Two other definitions quantifying the temporal variability of the simulated SAM are also used for cross-validation. One is the PC1 from EOF analysis of the SLP south of 20°S (PC1\_SLP; Thompson and Wallace, 2000); the other is the PC1 from EOF analysis of the zonal-mean zonal wind south of 10°S (PC1\_zmU; Lorenz and Hartmann, 2001). The Niño3.4 index is used to represent the ENSO variability. Spline interpolation is employed for the zonal-mean zonal wind at 850 hPa and then the latitude with maximum zonal wind is identified as the latitude of the eddy-driven jet.

The *t* statistic is used as the statistical significance test for the difference between the average values from two samples:

$$t = \frac{\overline{x_1} - \overline{x_2}}{\sqrt{(1/n_1 + 1/n_2)[(n_1 - 1)S_1^2 + (n_2 - 1)S_2^2]}/(n_1 + n_2 - 2)}, \quad (1)$$

**Table 1.** List of CMIP5 models used in this study and their horizontal and vertical resolutions. The abbreviations “nLat” and “nLon” mean the number of grids in the latitudinal and longitudinal direction, respectively. The short names for each model are listed in the last column.

Model name	Horizontal resolution (Lat × Lon)	Vertical resolution		
		Number of levels	Top level (hPa)	Short name
ACCESS1-0	145 × 192	17	10	A
ACCESS1-3	145 × 192	17	10	B
BCC-CSM1.1	64 × 128	17	10	C
BCC-CSM1.1(m)	160 × 320	17	10	D
BNU-ESM	64 × 128	17	10	E
CanAM4	64 × 128	22	1	F
CCSM4	192 × 288	17	10	G
CESM1-CAM5	192 × 288	17	10	H
CMCC-CM	240 × 480	17	10	I
CNRM-CM5	128 × 256	17	10	J
CSIRO-Mk3-6-0	96 × 192	18	5	K
EC-EARTH	160 × 320	16	20	L
FGOALS-G2.0	60 × 128	17	10	M
FGOALS-s2	108 × 128	17	10	N
GFDL-CM3	90 × 144	23	1	O
GFDL-HIRAM-C180	360 × 576	17	10	P
GFDL-HIRAM-C360	720 × 1152	17	10	Q
GISS-E2-R	90 × 144	17	10	R
HadGEM2-A	145 × 192	17	10	S
INMCM4	120 × 180	17	10	T
IPSL-CM5A-LR	96 × 96	17	10	U
IPSL-CM5A-MR	143 × 144	17	10	V
IPSL-CM5B-LR	96 × 96	17	10	W
MIROC5	128 × 256	17	10	X
MPI-ESM-LR	96 × 192	25	0.1	Y
MPI-ESM-MR	96 × 192	25	0.1	Z
MRI-CGCM3	160 × 320	23	0.1	a
NorESM1-M	96 × 144	17	10	b

where  $n_1$  and  $n_2$ ,  $x_1$  and  $x_2$ ,  $S_1$  and  $S_2$  represent the size, statistical average, and standard deviation of the two samples, respectively. Under the null hypothesis assumption that the difference between the two samples is zero, the statistic follows the  $t$  distribution with degrees of freedom of  $n + m - 2$  (Wilks, 2006).

The Theil–Sen nonparametric estimation is used to estimate the linear trend, which is defined as the median of the slopes between all data pairs. It is insensitive to outliers and thus a robust estimate of linear trends (Theil, 1950; Sen, 1968). Suppose the time series of the variable of interest  $y$  is available, the Theil–Sen estimation of its linear trend  $L$  is expressed as:

$$L = \text{Median} \left\{ \frac{y_j - y_i}{j - i} \right\}, \quad \forall i < j, \quad (2)$$

where  $y_i$  is the  $i$ th value of  $y$ . The significance of the linear trend is assessed using the Mann–Kendall nonparametric test.

### 3. Intermodel spread of the simulated austral winter SAM trend

The observed spatial pattern of the SAM in the zonal wind field is quantified by the EOF1 of the zonal-mean zonal wind south of 10°S (Fig. 1a). A positive SAM phase corresponds to stronger and weaker westerlies at around 60°S and 40°S, respectively. The climatological position of the eddy-driven jet is at around 50°S. The positive phase of the SAM corresponds to a poleward shift of the eddy-driven jet. The SAM activity reflects a seesaw relationship between the SLP in middle and high latitudes, which can be seen from the observed cross-correlation of zonal-mean SLP among different latitudes (Fig. 1c). During the period of interest, 1979–2008, consistency exists among different definitions of the SAMI (Fig. 1b). Due to the lack of reliability in describing the temporal variability of the SAM before the satellite era, the station-based index of the SAM proposed by Marshall (2003) is used to represent the temporal variability of the observed SAMI. The 30-year sliding trend of the JJA SAMI exhibits a strengthening characteristic and

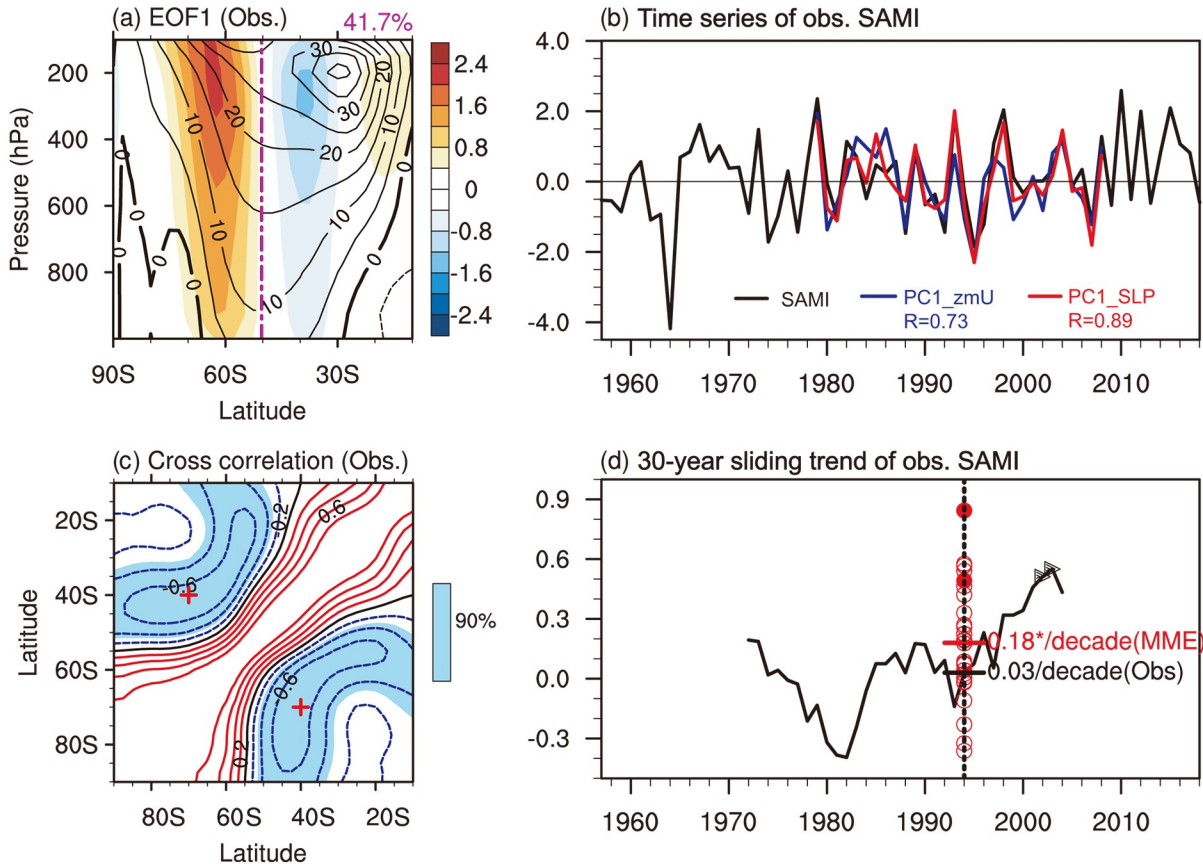


**Fig. 1.** The (a) EOF1 (shading; units:  $\text{m s}^{-1}$ ) and climatology (contours; units:  $\text{m s}^{-1}$ ) of zonal-mean zonal wind from reanalysis. The number in the top-right corner is the explained variance of EOF1. The purple dashed line marks the climatological position of the eddy-driven jet. (b) Time series of the observed SAMI proposed by Marshall (2003). Also shown are other definitions of the SAMI and their correlation coefficients with the SAMI-Marshall index during the period of interest (1979–2008). (c) Cross correlation of zonal-mean SLP among different latitudes (contours) from reanalysis, with the 90% confidence level shown by the shading. The cross symbols mark 40°S and 70°S. (d) The 30-year sliding trend of observed SAMI (black curve). The triangles indicate values significant at the 90% confidence level. For the period 1979–2008, the trends of the simulated SAMI from 28 models are shown as red circles. The solid and open circles indicate significant and non-significant values at the 90% confidence level. The red and black horizontal lines mark the MME and observed values for 1979–2008.

becomes significant at the 90% confidence level in recent years (Fig. 1d). The trend during 1979–2008 is  $0.03 (10 \text{ yr})^{-1}$ , showing that rare long-term changes occur in observation during this period.

Models perform differently in simulating the JJA SAMI trend during 1979–2008. Specifically, 22 out of 28 models simulate a positive SAMI trend, and a negative trend exists in 6 models (Fig. 1d). The positive trend is significant at the 90% confidence level in GFDL-CM3 [ $0.49 (10 \text{ yr})^{-1}$ ] and GFDL-HIRAM-C180 [ $0.84 (10 \text{ yr})^{-1}$ ]. The strongest negative trend occurs in MPI-ESM-LR [ $-0.36 (10 \text{ yr})^{-1}$ ]. The intermodel standard deviation for the JJA SAM trend,  $0.28 (10 \text{ yr})^{-1}$ , is even larger than that of the multimodel ensemble (MME) [ $0.18 (10 \text{ yr})^{-1}$ ]. Figure 2a shows the time series of the SAMI from individual models and the MME. Two other definitions quantifying the temporal variability of the simulated SAM are also used for cross-validation. The correlation between SAMI and PC1\_zmU and PC1\_SLP are significant (Fig. 2a). The conditional MME

(CMME; Yu et al., 2019) of the five models with the highest (lowest) SAMI trend is referred to as CMME1 (CMME2). CMME1 includes BCC-CSM1-1-M, EC-EARTH, GFDL-CM3, GFDL-HIRAM-C180, and MIROC5; CMME2 includes BNU-ESM, CCSM4, INMCM4, MPI-ESM-LR, and MPI-ESM-MR. Long-term changes in SAMI from CMME1 and CMME2 exhibit opposite trend (Fig. 2b). The trend from CMME1 is  $0.33 (10 \text{ yr})^{-1}$  (significant at the 90% level), while that from CMME2 is  $-0.19 (10 \text{ yr})^{-1}$  (significant at the 90% level). The distinction between CMME1 and CMME2 manifests the model difference in simulating the SAMI trend.

The trend in the zonal wind congruent with SAMI is obtained by first calculating the regression coefficients of the zonal wind on SAMI and then multiplying the result by the SAMI trend (Fig. 3). By doing this, the changes in SAMI are linearly projected on the zonal wind field. Observationally, the changes in zonal wind related to the SAM are relatively weak (Fig. 3a), because the observed SAMI trend is

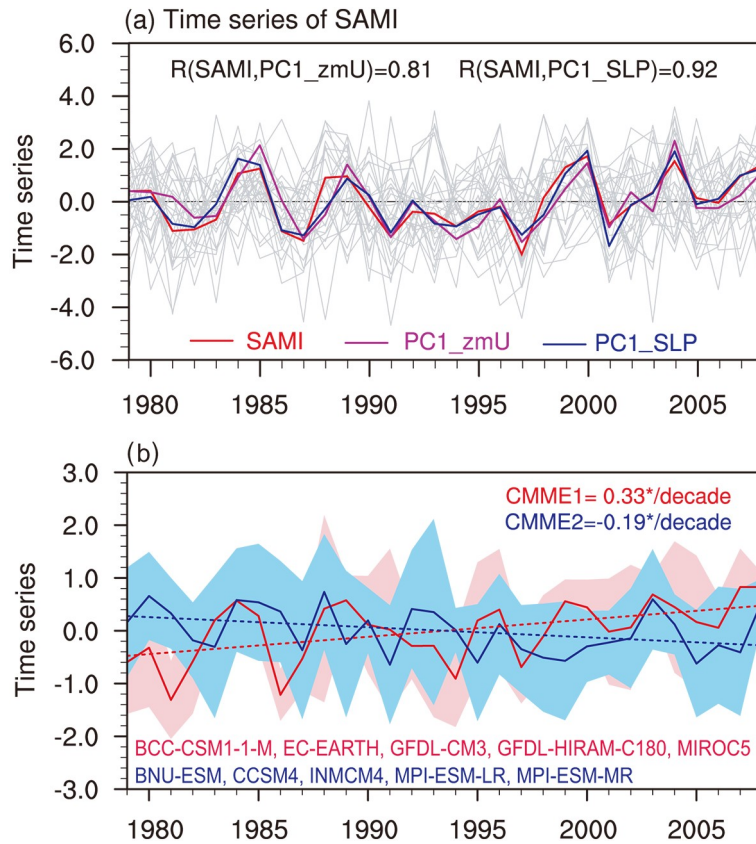


**Fig. 2.** (a) Time series of the simulated SAMI from individual models (gray) and the MME (red). PC1\_zmU (purple) and PC1\_SLP (blue) are also shown. (b) Time series of the simulated SAMI from CMME1 (red) and CMME2 (blue). The dotted lines represent linear trend components. The pink and light-blue shading illustrate the model spread quantified by one standard intermodel deviation.

non-significant (Fig. 1d). In the models from CMME1 (Figs. 3b–f), the westerlies congruent with the SAMI variability strengthen in high latitudes, while those in middle latitudes weaken, implying a poleward shift of the westerlies. In contrast, the zonal wind trend congruent with SAMI generally shows opposite changes in the models from CMME2, i.e., it weakens in high latitudes but strengthens in middle latitudes, suggesting an equatorward shift of the westerlies (Figs. 3g–k). The differences between CMME1 and CMME2 are clearly evident (Fig. 3l). Also shown in Fig. 3 are linear trends in total zonal wind. Similar to the trend congruent with SAMI, the westerly jet shifts poleward in CMME1 but exhibits an opposite equatorward shift in CMME2. This is reasonable because the SAM accounts for a large portion of circulation variability in the extratropics, and model spread in simulating the SAMI trend contributes to model spread in simulating changes in extratropical circulation.

To further investigate distinctions between CMME1 and CMME2 in simulated long-terms circulation changes, the differences in the linear trends of zonal-mean zonal wind (Fig. 4a) and geopotential height (Fig. 4b) are investigated. Accompanied by the poleward shift of the westerly jet, the polar vortex strengthens in CMME1. In contrast, the

polar vortex weakens in CMME2. Statistical significance testing suggests the differences between the two groups are significant at the 90% confidence level.

In the next section, potential factors underlying model differences in the simulated SAMI trend are investigated from the aspect of extratropical SST.

## 4. Role of the SOD

### 4.1. Linkage between the SOD and SAM

The distribution of correlation between SST and SAMI from the MME exhibits a zonal symmetric characteristic to a certain degree (Fig. 5a), which is more evident in Fig. 5b. The correlation between zonal-mean SST and SAMI shows that the strongest positive and negative correlation locates at around 40°S and 60°S, respectively. In fact, this dipole-like SST anomalies pattern resembles the dominant mode of Southern Hemisphere extratropical SST, which is referred to as the SOD (Zheng et al., 2018). The spatial pattern of the SOD is quantified by EOF1 of SST and zonal-mean SST south of 30°S (Figs. 5c and d). The corresponding PC1s are referred to as PC1\_SST and PC1\_zmSST. The explained variance of the SOD for zonal-mean SST is about

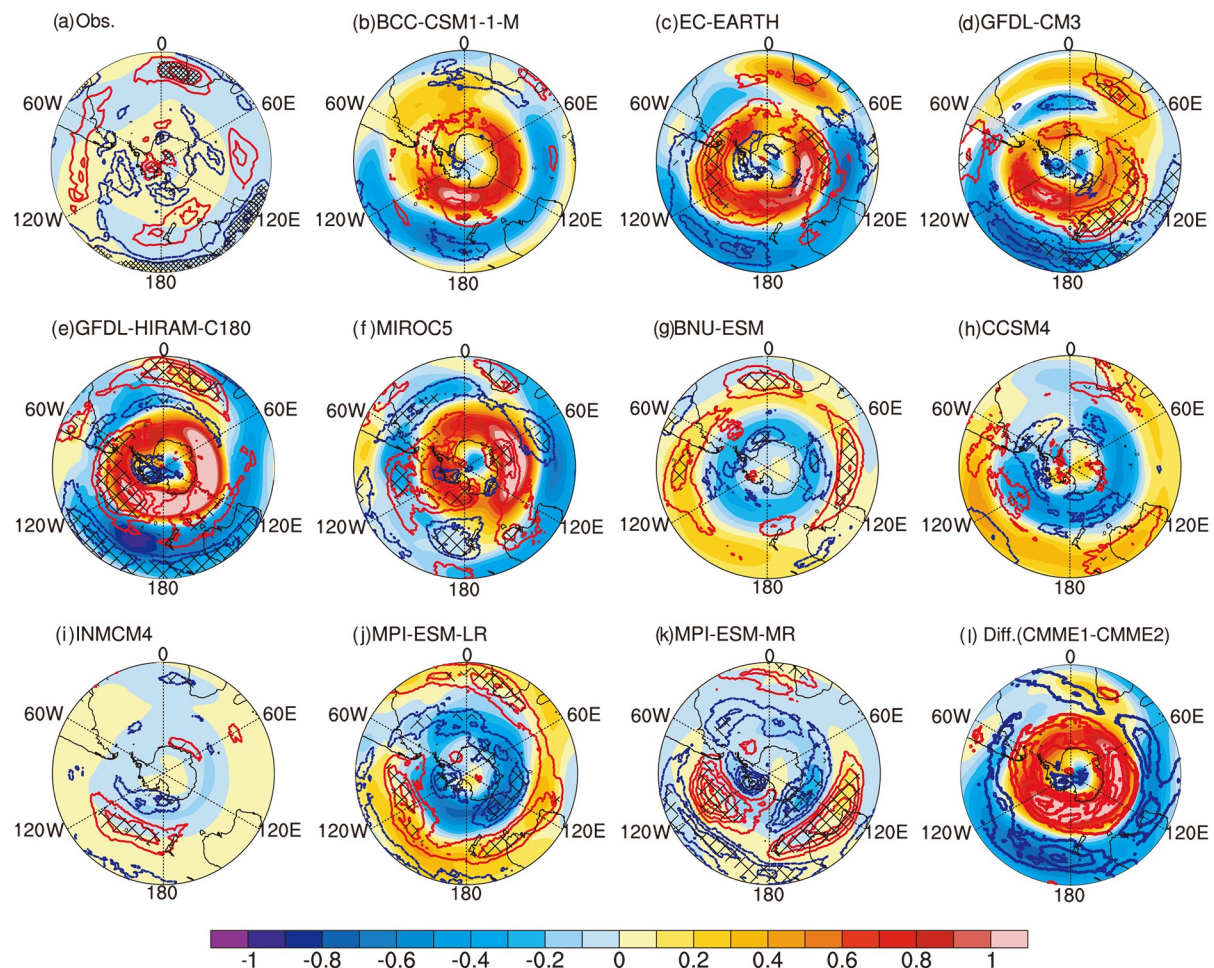


**Fig. 3.** Linear trend in vertically integrated tropospheric zonal wind [contours; units:  $\text{m s}^{-1} (10 \text{ yr})^{-1}$ ]. Red and blue contours show positive and negative values. The patches mark significance at the 90% confidence level. Also shown are the zonal wind trends congruent with SAMI [shading; units:  $\text{m s}^{-1} (10 \text{ yr})^{-1}$ ]: from (a) observations; (b–f) models in CMME1; (g–k) models in CMME2; and (l) the difference between CMME1 and CMME2.

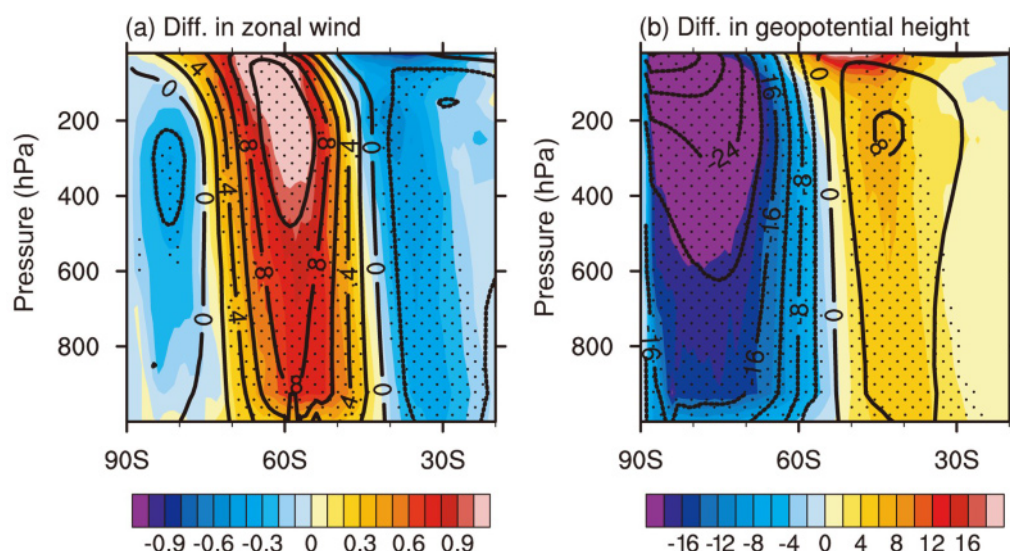


**Fig. 4.** (a) Difference in the linear trend of the zonal-mean zonal wind [units:  $\text{m s}^{-1} (10 \text{ yr})^{-1}$ ] between CMME1 and CMME2 (contours). Shading represents similar analysis but for the component in zonal wind congruent with SAMI [units:  $\text{m s}^{-1} (10 \text{ yr})^{-1}$ ]. Hatching indicates the difference is significant at the 90% confidence level. (b) As in (a) but for zonal-mean geopotential height [units:  $\text{hPa} (10 \text{ yr})^{-1}$ ].

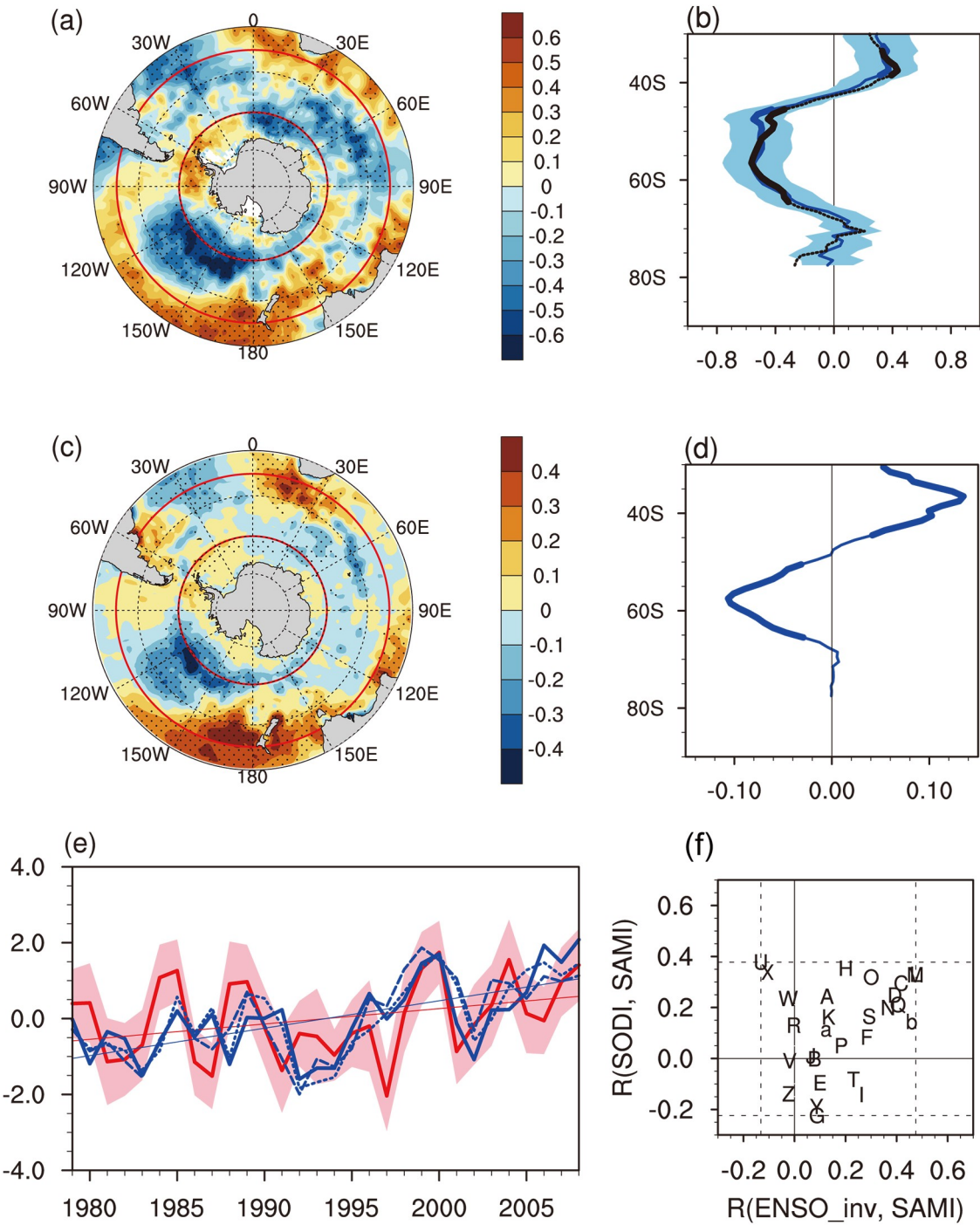


**Fig. 5.** (a) Correlation between SST and SAMI from the MME (shading). (b) As in (a) but for zonal-mean SST (blue curve). Also shown is the partial correlation after removing the contemporaneous ENSO signal (black). The shading illustrates the model spread quantified by one standard intermodel deviation. (c) EOF1 of SST south of 30°S (units: °C). (d) EOF1 of zonal-mean SST south of 30°S (units: °C). (e) Standardized time series of SAMI from the MME (red) and SODI (blue solid), with their linear trend components shown as thin lines. The blue dashed and blue dotted lines are PC1\_SST and PC1\_zmSST. (f) Correlation between SODI and SAMI (ordinate) versus the correlation between inverted ENSO index and SAMI (abscissa).

50%. To conveniently quantify the temporal variability of this dipole-like SST anomaly pattern, a SODI index is defined as the difference in SST between 40°S and 60°S. The SODI and PC1\_SST (PC1\_SSTzm) are highly correlated, with a correlation of 0.82 (0.91) (Fig. 5e). Standard-

ized time series of SODI and SAMI from the MME are shown in Fig. 5e. Covariability exists between SODI and SAMI, with a significant correlation of 0.42.

ENSO plays a role in influencing the SAM (L'Heureux and Thompson, 2006; Gong et al., 2010). The partial corre-

tion between the zonal-mean SST and SAM after linearly removing the contemporaneous ENSO is used to validate the linkage between the SST and SAM (Fig. 5b). Linearly removing ENSO slightly reduces the connection between the extratropical SST and SAM; the correlation remains significant at 40°S and 60°S. A model with good skill in simulating the ENSO–SAM relationship does not ensure a good performance in capturing the SOD–SAM relationship (Fig. 5f).

Therefore, the perturbation from ENSO on the model-simulated SOD–SAM relationship is not considered in the following analysis.

#### 4.2. *Intermodel diversity related to the SOD*

The correlation between the SST and SAMI from CMME1 is shown in Figs. 6a and b, in which the SOD structure is found: positive and negative correlation appear at

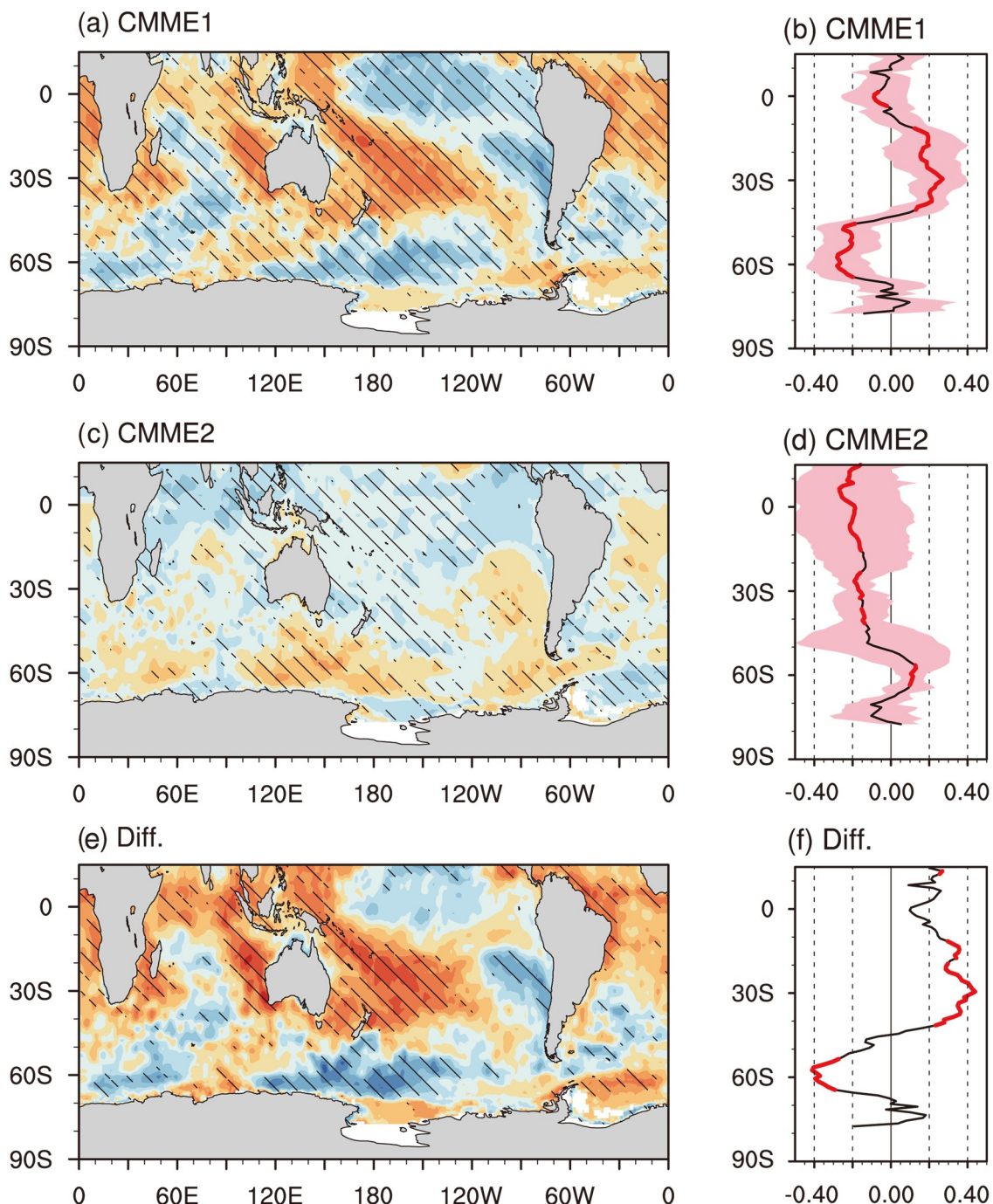


**Fig. 6.** Correlation between the SST and SAMI from (a) CMME1 and (c) CMME2. (b, d) As in (a, c) but for zonal-mean SST. Shading represents the intermodel spread quantified by one intermodel standard deviation. The patches in (a, c) and red curves in (b, d) indicate the locations where four out of five models have the same sign. (e, f) The difference between CMME1 and CMME2. The patches in (e) and red curves in (f) indicate the difference is statistically significant at the 90% confidence level.

around 40°S and 60°S, respectively. However, the dipole-like structure from CMME2 (Figs. 6c and d) shows an opposite phase: negative correlation exists at 40°S and positive correlation exists at 60°S. The difference between CMME1 and CMME2 is shown in Figs. 6e and f, illustrating that models with a higher SAMI trend (CMME1) are characterized by a stronger SOD–SAM connection.

The intermodel correlation between the SAMI trend and SST–SAMI relationship (Fig. 7a) is calculated as follows: (1) For a specific grid on the map, the intermodel correlation is calculated between two series: one series is the SAMI trend from 28 models; the other is the SST–SAMI correlation from 28 models. (2) Repeating this process at every grid, the distribution in Fig. 7a is then obtained. Note that the series of the SAMI trend is identical among the grids, but the series of the SST–SAMI correlation is grid-dependent. The stronger the SAMI trend, the higher (lower) the SST–SAMI correlation in middle (high) latitudes. That is, the stronger the SOD–SAM connection, the stronger the SAMI trend. The results for zonal-mean SST also suggest a dependence of the model-simulated SAMI changes on model skill in reflecting the SOD–SAM relationship (Fig. 7b). Also shown are results based on the other two SAM definitions, PC1\_SLP and PC1\_zmU. The consistency among the three curves suggests that the intermodel relationship in Fig. 7b is insensitive to the SAM definition.

Figure 8a shows a scatter diagram of the trend in SAMI against the SOD–SAM relationship. The correlation between the ordinate and abscissa data is 0.69, implying model performance in simulating the SOD–SAM relationship accounts for 48% of the intermodel variance in simulating the SAMI trend. Conducting similar analysis using other SAMI definitions, the linkage between the simulated SOD–SAM relationship and SAMI trend is also clear. The explained variances using PC1\_SLP (Fig. 8b) and PC1\_zmU (Fig. 8c) are 55% and 30%, respectively. On average, model performance in simulating the SOD–SAM rela-

tionship accounts for about 40% of the intermodel variance in simulating the SAM trend in the AMIP runs.

Previous studies have found that the SOD plays a role in influencing extratropical circulation by influencing baroclinicity. Specifically, a positive SOD phase corresponds to increased (decreased) baroclinicity south (north) of 50°S. According to eddy–zonal mean flow interaction theory, anomalies in baroclinicity tend to produce anomalous eddy momentum flux convergence (divergence) south (north) of 50°S, resulting in strengthened (weakened) westerly flow south (north) of 50°S, leading to a positive SAM phase (Zheng et al., 2015, 2018). Figure 8d shows the intermodel correlation between the SAMI trend and the trend in the meridional gradient of potential temperature, which is a measure of baroclinicity. A model with a stronger SAMI trend is characterized by stronger and weaker baroclinicity at around 60°S and 40°S, respectively.

The intermodel correlation between the trend in geopotential height and the SOD–SAM relationship shows that models with a closer SOD–SAM linkage tend to simulate a larger deepening trend of the polar vortex (Fig. 8e). Since deepening of the polar vortex is a manifestation of the increasing trend of SAMI, Fig. 8 further verifies that the simulated influence of the SOD on the SAM acts as one source of model spread in depicting long-term changes in the SAM.

## 5. Discussion and conclusions

The performances of state-of-the-art models in simulating long-term changes in the SAM and related Antarctic climate during the historical period have been found to be improved from CMIP3 to CMIP5 (Gillett and Fyfe, 2013; Wang, 2013; Zheng et al., 2013; Wang et al., 2015). However, the potential sources of the intermodel spread in simulating the SAM trend are not well understood. Considering the role of the SAM in regulating Southern Hemisphere extratropical circulation, model uncertainty in simulating

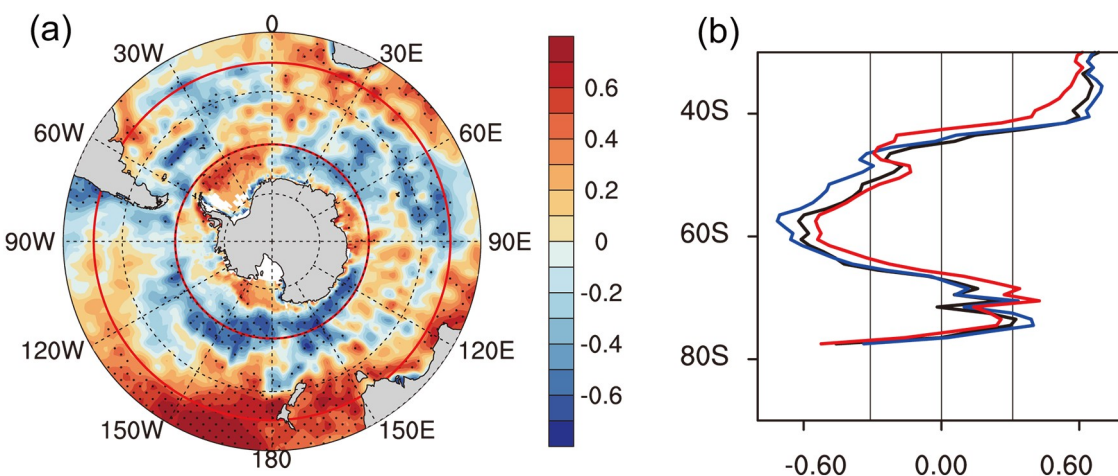


**Fig. 7.** (a) Intermodel correlation between the SAMI trend and SST–SAMI correlation. Stippling represents the 90% confidence level. (b) As in (a) but for the zonal-mean SST (black). The blue and red curves show results when the SAMI is replaced by PC1\_SLP and PC1\_zmU.

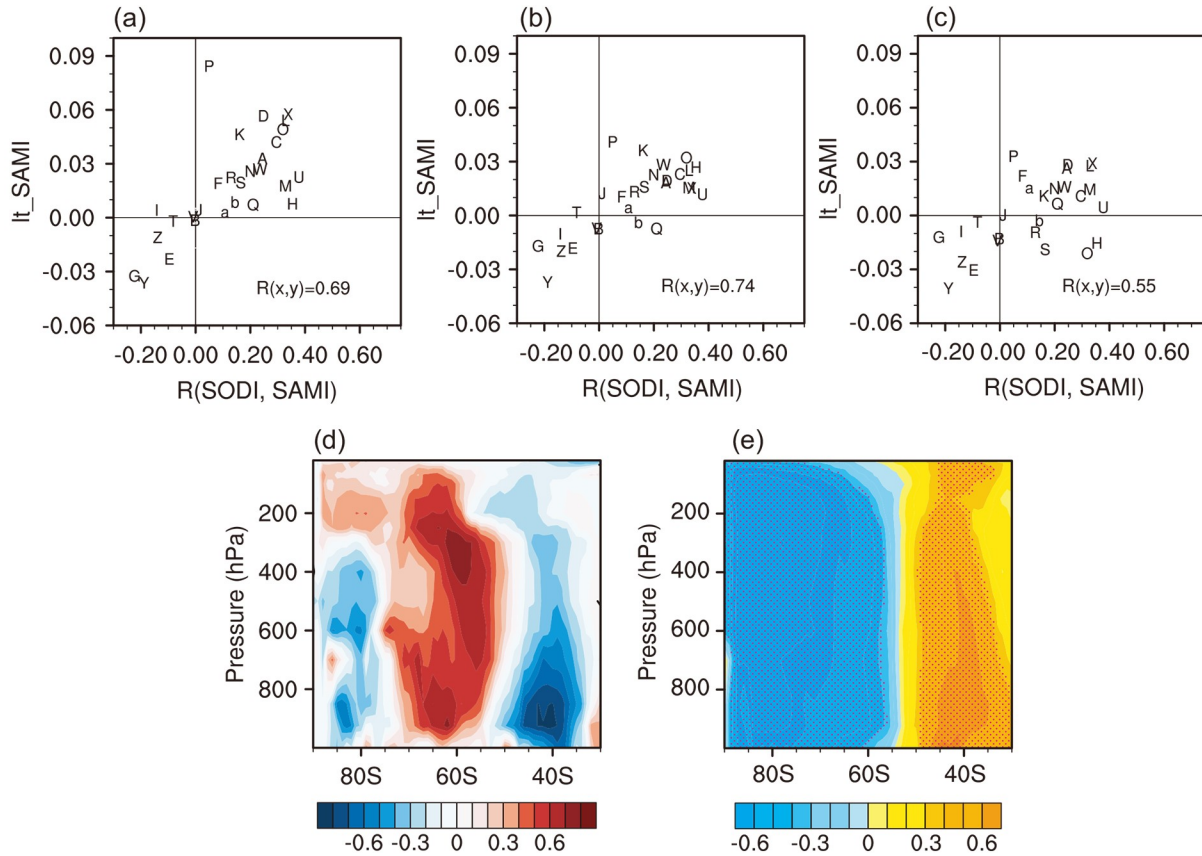


**Fig. 8.** (a) Scatterplot of the trend in SAMI (ordinate) against the SODI–SAMI correlation (abscissa). (b, c) As in (a) but the SAMI is replaced by (b) PC1\_SLP and (c) PC1\_zmU. (d) Intermodel correlation between the trend in SAMI and the trend in the meridional gradient of potential temperature. (e) Intermodel correlation between the trend in geopotential height and the SODI–SAMI correlation. Stippling marks the 90% confidence level.

the SAM trend contributes to uncertainty in the simulated changes of extratropical climate. Examining factors responsible for the intermodel diversity in the SAM's long-term changes may provide information for improving the simulation of extratropical climate.

Using AMIP simulations from 28 models archived in CMIP5, this study shows that the intermodel diversity in the trend of the austral winter (JJA) SAMI is non-negligible, with the intermodel standard deviation of  $0.28 (10 \text{ yr})^{-1}$  being larger than the MME of  $0.18 (10 \text{ yr})^{-1}$ . The model spread in simulating the SAMI trend contributes to the model spread in depicting the changes in extratropical circulation. The polar jet shifts toward the Antarctic and the polar vortex strengthens in models with significant positive SAM trend, while in models with significant negative SAM trend, polar jet exhibits equatorward shift and polar vortex weakens. The differences between the two groups are significant.

The role of SOD-like SST anomalies in influencing the SAM is found in AMIP simulations, which is consistent with previous studies (Liu et al., 2015; Zheng et al., 2015). Model performance in simulating the SAMI trend is linked with model skill in reflecting the SOD–SAM relationship. Models with stronger correlation between the SOD and SAM tend to simulate a stronger SAM trend, and vice versa. Model performance in simulating the SOD–SAM rela-

tionship accounts for about 40% of the intermodel variance in simulating the SAM trend in the AMIP runs. The ability of models in depicting internal processes of the climate system acts as one source of model uncertainty in simulating the response of the climate to external forcing. The above result is a manifestation of the fact that the direct effect of external forcing on climate changes might be influenced by internal processes in the climate system (Cane et al., 1997).

Focusing on the responses of atmospheric circulation to SST anomalies, this study only used AMIP models. In the real climate system, there is a two-way coupling between the atmosphere and ocean, i.e., the SAM also plays a role in influencing the SOD (e.g., Wang and Fan, 2005; Sen Gupta and England, 2006; Fan, 2007; Yang et al., 2007; Bian et al., 2010; Shi et al., 2013; Wu and Francis, 2019; Wu et al., 2020; Yuan et al., 2020). Using atmosphere–ocean coupled experiments to verify the contribution of SOD–SAM coupling to model uncertainty helps in further understanding the reasons underlying the intermodel diversity. As outputs from CMIP6 have become available, the relationship between the simulated SAM trend and model performance in capturing the SOD–SAM relationship needs to be further validated using these latest models.

Aside from the extratropical SOD, tropical SST anomalies (e.g., ENSO) also plays a role in influencing the SAM

variability. The teleconnection from lower latitudes exhibits its seasonal features. Investigating the seasonality of the SOD–SAM relationship in further study will be helpful for understanding extratropical air–sea interactions. Furthermore, whether the role of the SOD–SAM relationship in influencing the SAM trend is seasonally dependent remains an open question.

**Acknowledgements.** This work was jointly supported by the Strategic Priority Research Program of the Chinese Academy of Sciences (Grant No. XDA19070402), a National Key Research and Development Project (Grant No. 2018YFA0606404), and the National Natural Science Foundation of China (Grant Nos. 41790474 and 41775090). We acknowledge the World Climate Research Programme's Working Group on Coupled Modelling, which is responsible for CMIP, and we thank the climate modeling groups for producing and making available their model output. The authors appreciate the comments of the two anonymous reviewers and the editor.

## REFERENCES

Bian, L. G., X. C. Lin, and L. Xia, 2010: Antarctica sea-ice oscillation and its possible impact on monsoon of South Sea. *Chinese Journal of Polar Science*, **21**, 11–21.

Cane, M. A., A. C. Clement, A. Kaplan, Y. Kushnir, D. Pozdnyakov, R. Seager, S. E. Zebiak, and R. Murtugudde, 1997: Twentieth-century sea surface temperature trends. *Science*, **275**, 957–960, <https://doi.org/10.1126/science.275.5302.957>.

Fan, K., 2007: Zonal asymmetry of the Antarctic Oscillation. *Geophys. Res. Lett.*, **34**, L02706, <https://doi.org/10.1029/2006GL028045>.

Fogt, R. L., J. M. Jones, and J. Renwick, 2012: Seasonal zonal asymmetries in the southern annular mode and their impact on regional temperature anomalies. *J. Climate*, **25**, 6253–6270, <https://doi.org/10.1175/JCLI-D-11-00474.1>.

Gillett, N. P., and J. C. Fyfe, 2013: Annular mode changes in the CMIP5 simulations. *Geophys. Res. Lett.*, **40**, 1189–1193, <https://doi.org/10.1002/grl.50249>.

Gong, D. Y., and S. W. Wang, 1999: Definition of Antarctic Oscillation index. *Geophys. Res. Lett.*, **26**, 459–462, <https://doi.org/10.1029/1999GL900003>.

Gong, T. T., S. B. Feldstein, and D. H. Luo, 2010: The impact of ENSO on wave breaking and southern annular mode events. *J. Atmos. Sci.*, **67**, 2854–2870, <https://doi.org/10.1175/2010JAS3311.1>.

Hartmann, D. L., and F. Lo, 1998: Wave-driven zonal flow vacillation in the southern Hemisphere. *J. Atmos. Sci.*, **55**, 1303–1315, [https://doi.org/10.1175/1520-0469\(1998\)055<1303:WDZFVI>2.0.CO;2](https://doi.org/10.1175/1520-0469(1998)055<1303:WDZFVI>2.0.CO;2).

Hu, C. D., Q. G. Wu, S. Yang, Y. H. Yao, D. Chan, Z. N. Li, and K. Q. Deng, 2016: A linkage observed between austral autumn Antarctic Oscillation and preceding Southern Ocean SST anomalies. *J. Climate*, **29**, 2109–2122, <https://doi.org/10.1175/JCLI-D-15-0403.1>.

Kang, S. M., I. M. Held, D. M. W. Frierson, and M. Zhao, 2008: The response of the ITCZ to extratropical thermal forcing: Idealized slab-ocean experiments with a GCM. *J. Climate*, **21**, 3521–3532, <https://doi.org/10.1175/2007JCLI2146.1>.

Kang, S. M., D. M. W. Frierson, and I. M. Held, 2009: The tropical response to extratropical thermal forcing in an idealized GCM: The importance of radiative feedbacks and convective parameterization. *J. Atmos. Sci.*, **66**, 2812–2827, <https://doi.org/10.1175/2009JAS2924.1>.

Kidson, J. W., and I. G. Watterson, 1999: The structure and predictability of the “high-latitude mode” in the CSIRO9 general circulation model. *J. Atmos. Sci.*, **56**, 3859–3873, [https://doi.org/10.1175/1520-0469\(1999\)056<3859:TSAPOT>2.0.CO;2](https://doi.org/10.1175/1520-0469(1999)056<3859:TSAPOT>2.0.CO;2).

Kidston, J., and E. P. Gerber, 2010: Intermodel variability of the poleward shift of the austral jet stream in the CMIP3 integrations linked to biases in 20th century climatology. *Geophys. Res. Lett.*, **37**, L09708, <https://doi.org/10.1029/2010GL042873>.

Kidston, J., J. A. Renwick, and J. McGregor, 2009: Hemispheric-scale seasonality of the Southern Annular Mode and impacts on the climate of New Zealand. *J. Climate*, **22**, 4759–4770, <https://doi.org/10.1175/2009JCLI2640.1>.

Kushnir, Y., W. A. Robinson, I. Bladé, N. M. J. Hall, S. Peng, and R. Sutton, 2002: Atmospheric GCM response to extratropical SST anomalies: Synthesis and evaluation. *J. Climate*, **15**, 2233–2256, [https://doi.org/10.1175/1520-0442\(2002\)015<2233:AGRTE>2.0.CO;2](https://doi.org/10.1175/1520-0442(2002)015<2233:AGRTE>2.0.CO;2).

Lau, N. C., and M. J. Nath, 1990: A general circulation model study of the atmospheric response to extratropical SST anomalies observed in 1950–79. *J. Climate*, **3**, 965–989, [https://doi.org/10.1175/1520-0442\(1990\)003<0965:AGCM>2.0.CO;2](https://doi.org/10.1175/1520-0442(1990)003<0965:AGCM>2.0.CO;2).

L'Heureux, M. L., and D. W. J. Thompson, 2006: Observed relationships between the El Niño–southern Oscillation and the extratropical zonal-mean circulation. *J. Climate*, **19**, 276–287, <https://doi.org/10.1175/JCLI3617.1>.

Li, J. P., and J. X. L. Wang, 2003: A modified zonal index and its physical sense. *Geophys. Res. Lett.*, **30**, 1632, <https://doi.org/10.1029/2003GL017441>.

Li, N., and G. McGregor, 2017: Linking interannual river flow variability across New Zealand to the southern Annular Mode, 1979–2011. *Hydrological Processes*, **31**, 2261–2276, <https://doi.org/10.1002/hyp.11184>.

Li, S. L., M. P. Hoerling, and S. L. Peng, 2006: Coupled ocean–atmosphere response to Indian Ocean warmth. *Geophys. Res. Lett.*, **33**, L07713, <https://doi.org/10.1029/2005GL025558>.

Lim, E. P., H. H. Hendon, J. M. Arblaster, F. Delage, H. Nguyen, S. K. Min, and M. C. Wheeler, 2016: The impact of the southern annular mode on future changes in Southern Hemisphere rainfall. *Geophys. Res. Lett.*, **43**, 7160–7167, <https://doi.org/10.1002/2016GL069453>.

Liu, T., J. P. Li, and F. Zheng, 2015: Influence of the boreal autumn southern annular mode on winter precipitation over land in the northern Hemisphere. *J. Climate*, **28**, 8825–8839, <https://doi.org/10.1175/JCLI-D-14-00704.1>.

Lorenz, D. J., and D. L. Hartmann, 2001: Eddy-zonal flow feedback in the Southern Hemisphere. *J. Atmos. Sci.*, **58**, 3312–3327, [https://doi.org/10.1175/1520-0469\(2001\)058<3312:EZFF>2.0.CO;2](https://doi.org/10.1175/1520-0469(2001)058<3312:EZFF>2.0.CO;2).

Marshall, A. G., M. A. Hemer, H. H. Hendon, and K. L. McInnes, 2018: Southern annular mode impacts on global ocean surface waves. *Ocean Modelling*, **129**, 58–74, <https://doi.org/10.1016/j.ocemod.2018.07.007>.

Marshall, G. J., 2003: Trends in the southern annular mode from

observations and reanalyses. *J. Climate*, **16**, 4134–4143, [https://doi.org/10.1175/1520-0442\(2003\)016<4134:TIT-SAM>2.0.CO;2](https://doi.org/10.1175/1520-0442(2003)016<4134:TIT-SAM>2.0.CO;2).

Nakamura, H., T. Sampe, A. Goto, W. Ohfuchi, and S. P. Xie, 2008: On the importance of midlatitude oceanic frontal zones for the mean state and dominant variability in the tropospheric circulation. *Geophys. Res. Lett.*, **35**, L15709, <https://doi.org/10.1029/2008GL034010>.

Nan, S. L., and J. P. Li, 2003: The relationship between the summer precipitation in the Yangtze River valley and the boreal spring Southern Hemisphere annular mode. *Geophys. Res. Lett.*, **30**, 2266, <https://doi.org/10.1029/2003GL018381>.

Sampe, T., H. Nakamura, A. Goto, and W. Ohfuchi, 2010: Significance of a midlatitude SST frontal zone in the formation of a storm track and an eddy-driven westerly jet. *J. Climate*, **23**, 1793–1814, <https://doi.org/10.1175/2009JCLI3163.1>.

Sen Gupta, A., and M. H. England, 2006: Coupled ocean-atmosphere-ice response to variations in the southern annular mode. *J. Climate*, **19**, 4457–4486, <https://doi.org/10.1175/JCLI3843.1>.

Sen Gupta, A., and M. H. England, 2007: Coupled ocean-atmosphere feedback in the southern annular mode. *J. Climate*, **20**, 3677–3692, <https://doi.org/10.1175/JCLI4200.1>.

Sen, P. K., 1968: Estimates of the regression coefficient based on Kendall's tau. *Journal of the American Statistical Association*, **63**, 1379–1389.

Shi, J. X., Z. Q. Dong, and H. X. Chen, 2013: Progress of Chinese research in physical oceanography of the Southern Ocean. *Advances in Polar Science*, **24**, 86–97, <https://doi.org/10.3724/SP.J.1085.2013.00086>.

Swart, N. C., J. C. Fyfe, N. Gillett, and G. J. Marshall, 2015: Comparing trends in the Southern Annular Mode and surface westerly jet. *J. Climate*, **28**, 8840–8859, <https://doi.org/10.1175/JCLI-D-15-0334.1>.

Taylor, K. E., R. J. Stouffer, and G. A. Meehl, 2012: An overview of CMIP5 and the experiment design. *Bull. Amer. Meteor. Soc.*, **93**, 485–498, <https://doi.org/10.1175/BAMS-D-11-00094.1>.

Theil, H., 1950: A rank-invariant method of linear and polynomial regression analysis, I. *Proceedings of the Koninklijke Nederlandse Akademie Wetenschappen, Series A Mathematical Sciences*, **53**, 386–392.

Thompson, D. W. J., and J. M. Wallace, 2000: Annular modes in the extratropical circulation. Part I: Month-to-month variability. *J. Climate*, **13**, 1000–1016, [https://doi.org/10.1175/1520-0442\(2000\)013<1000:AMITEC>2.0.CO;2](https://doi.org/10.1175/1520-0442(2000)013<1000:AMITEC>2.0.CO;2).

Thompson, D. W. J., S. Solomon, P. J. Kushner, M. H. England, K. M. Grise, and D. J. Karoly, 2011: Signatures of the Antarctic ozone hole in Southern Hemisphere surface climate change. *Nature Geoscience*, **4**, 741–749, <https://doi.org/10.1038/ngeo1296>.

Turner, J., and Coauthors, 2005: Antarctic climate change during the last 50 years. *International Journal of Climatology*, **25**, 279–294, <https://doi.org/10.1002/joc.1130>.

Wang, H. J., and K. Fan, 2005: Central-North China precipitation as reconstructed from the Qing Dynasty: Signal of the Antarctic Atmospheric Oscillation. *Geophys. Res. Lett.*, **32**, L24705, <https://doi.org/10.1029/2005GL024562>.

Wang, Z. M., 2013: On the response of southern Hemisphere subpolar gyres to climate change in coupled climate models. *J. Geophys. Res.*, **118**, 1070–1086, <https://doi.org/10.1002/jgrc.20111>.

Wang, Z. M., X. D. Zhang, Z. Y. Guan, B. Sun, X. Yang, and C. Y. Liu, 2015: An atmospheric origin of the multi-decadal bipolar seesaw. *Scientific Reports*, **5**, 8909, <https://doi.org/10.1038/srep08909>.

Wilks, D. S., 2006: *Statistical Methods in the Atmospheric Sciences*. 3rd ed., Academic Press.

Wu, B. Y., and J. A. Francis, 2019: Summer Arctic cold anomaly dynamically linked to East Asian heat waves. *J. Climate*, **32**, 1137–1150, <https://doi.org/10.1175/JCLI-D-18-0370.1>.

Wu, Q. G., and X. D. Zhang, 2011: Observed evidence of an impact of the Antarctic sea ice dipole on the Antarctic Oscillation. *J. Climate*, **24**, 4508–4518, <https://doi.org/10.1175/2011JCLI3965.1>.

Wu, Y., Z. M. Wang, C. Y. Liu, and X. Lin, 2020: Impacts of high-frequency atmospheric forcing on Southern Ocean circulation and Antarctic sea ice. *Adv. Atmos. Sci.*, **37**, 515–531, <https://doi.org/10.1007/s00376-020-9203-x>.

Wu, Z. W., J. P. Li, B. Wang, and X. H. Liu, 2009: Can the southern Hemisphere annular mode affect China winter monsoon? *J. Geophys. Res.*, **114**, D11107, <https://doi.org/10.1029/2008JD011501>.

Xiao, B., Y. Zhang, X. Q. Yang, and Y. Nie, 2016: On the role of extratropical air-sea interaction in the persistence of the Southern Annular Mode. *Geophys. Res. Lett.*, **43**, 8806–8814, <https://doi.org/10.1002/2016GL070255>.

Yang, H. J., and L. Wang, 2011: Tropical oceanic response to extratropical thermal forcing in a coupled climate model: A comparison between the Atlantic and Pacific Oceans. *J. Climate*, **24**, 3850–3866, <https://doi.org/10.1175/2011JCLI3927.1>.

Yang, X. Y., D. X. Wang, J. Wang, and R. X. Huang, 2007: Connection between the decadal variability in the southern Ocean circulation and the Southern Annular Mode. *Geophys. Res. Lett.*, **34**, L16604, <https://doi.org/10.1029/2007GL030526>.

Yu, M., J. P. Li, F. Zheng, X. F. Wang, and J. Y. Zheng, 2019: Simulating the IPOD, East Asian summer monsoon, and their relationships in CMIP5. *Theor. Appl. Climatol.*, **135**, 1307–1322, <https://doi.org/10.1007/s00704-018-2442-4>.

Yuan, Z. X., J. Qin, S. L. Li, S. J. Huang, and Y. Mbululo, 2020: Impact of spring AAO on summertime precipitation in the North China Part: Observational analysis. *Asia-Pacific Journal of Atmospheric Sciences*, <https://doi.org/10.1007/s13143-019-00157-2>.

Zhang, Y., X. Q. Yang, Y. Nie, and G. Chen, 2012: Annular mode-like variation in a multilayer quasigeostrophic model. *J. Atmos. Sci.*, **69**, 2940–2958, <https://doi.org/10.1175/JAS-D-11-0214.1>.

Zheng, F., J. P. Li, R. T. Clark, and H. C. Nnamchi, 2013: Simulation and projection of the southern Hemisphere Annular Mode in CMIP5 models. *J. Climate*, **26**, 9860–9879, <https://doi.org/10.1175/JCLI-D-13-00204.1>.

Zheng, F., J. P. Li, L. Wang, F. Xie, and X. F. Li, 2015: Cross-seasonal influence of the December–February southern Hemisphere annular mode on March–May meridional circulation and precipitation. *J. Climate*, **28**, 6859–6881, <https://doi.org/10.1175/JCLI-D-14-00515.1>.

Zheng, F., J. P. Li, F. Kucharski, R. Q. Ding, and T. Liu, 2018: Dominant SST mode in the southern Hemisphere extratropics and its influence on atmospheric circulation. *Adv. Atmos. Sci.*, **35**, 881–895, <https://doi.org/10.1007/s00376-017-7162-7>.